Creation of Piezoelectricity in Quadruple Perovskite Oxides by Harnessing Cation Defects and Their Application in Piezo- Photocatalysis

Thomsen, Peng Chen, Kai Wang, Xiangyu Guo,* Chen Han, Lihong Liu, Zhiliang Wang, Lars Zongping Shao, Xudong Wang, Fang Xie, Gang Liu, Lianzhou Wang, and Shaomin Liu*

ABSTRACT: Quadruple perovskite oxides have received extensive attention in electronics and catalysis, owing to their cation-ordering structure and intriguing physical properties. However, their repertoires still remain limited. In particular, piezoelectricity from quadruple perovskites has been rarely reported due to the frustrated symmetry-breaking transition in A-site-ordered perovskite structures, disabling their piezoelectric applications. Herein, we report a feasible strategy to achieve piezoelectricity in CaCu3Ti4O12 (CCTO) quadruple perovskite via cation defect engineering, specifically through a thermal-driven selective cation exsolution strategy to introduce Cu vacancies. The introduction of Cu point defects in CCTO locally destabilizes the constrained tilted TiO6 octahedra framework, relaxing the octahedral tilting and inducing structural heterogeneity which, in turn, disrupts the high symmetry of the pristine cubic phase. As a result, the defective CCTO with localized asymmetry exhibits intense polarization and a robust piezoelectricity of 7 pC N^{-1} . The created piezoelectricity is further validated by its application as a piezo-photocatalyst, enabling efficient charge separation and transfer with a 2.5-times increment in the lifetime of photoexcitations. This enhancement leads to a 3.86- and 31-fold increase in the production of hydrogen peroxide and reactive oxygen species compared with individual piezocatalysis and photocatalysis, respectively. This study establishes a pathway to engineer piezoelectricity in quadruple perovskites, potentially unlocking a wide range of applications in modern microelectronics beyond the demonstrated piezo-photocatalysis.

KEYWORDS: quadruple perovskite oxide, piezoelectricity, cation defect, polarization, piezo-photocatalysis, hydrogen peroxide

Perovskite oxides ABO3 and their derivatives exhibit a rich variety of physicochemical properties, such as piezoelectricity, ferroelectricity, semiconductivity, and catalysis, attributed to their compositional and structural flexibility.1−3 Among diverse derivatives, a special group of A-site cation-ordered perovskite oxides with a nominal composition of AÀ 3B4O12, known as quadruple perovskite oxides, has garnered extensive attention for many advanced electronic applications because of their interesting physical properties in magnetoresistance, high permittivity, charge/orbital/magnetic ordering, and ferrimagnetic half-metallicity.4−7 Different from simple ABO3 perovskites, where the 12-coordinated A-site often accommodates large ionic alkali, alkaline-earth, or lanthanide elements, three quarters of the A-site cations in quadruple perovskite are substituted by small transition metals (i.e., Cu2+ or Mn3+ at the À -site).8 These small transition metals in the À -sites arrange orderly and exhibit a square-planar coordination (À O4) perpendicular to each other, causing substantial tilting of BO6 octahedrons (Figure 1a,b). Importantly, such a special arrangement of transition metals at the À -site and the À -B electronic interactions gives rise to the distinctive properties of quadruple perovskites. For example, the perpendicular alignment of CuO4 squares provides direct-exchange interaction between the nearest Cu2+ spins, inducing ferromagnetic property in CaCu3Ge4O12 quadruple perovskite.7 Moreover, the À -B (Cu−Fe) intersite charge transfer in the ACu3Fe4O12 system could trigger charge disproportionation of Fe, resulting in near-zero thermal expansion behavior of the material in certain temperature ranges.9

In spite of the interesting properties achieved, the repertoire of quadruple perovskites is still quite restricted compared to ABO3 simple perovskites.10−13 In particular, piezoelectric and ferroelectric properties, which are essential for many modern microelectronic and optoelectronic applications, are rarely observed in quadruple perovskites because of their highly stable and symmetric crystallographic structure. Specifically, the square-planar coordination for À -site restrains the flexibility of BO6 octahedra via the À -O bond, enhancing the rigidity of the entire octahedral framework, consequently forming a robust centrosymmetric crystal structure.6 An intriguing observation is that the majority of the reported quadruple perovskite oxides adopt the ideal cubic phase with a space group of Im$\bar{3}$. 14 Therefore, breaking the high symmetry of quadruple perovskites to achieve piezoelectricity and ferroelec□tricity, for the purpose of enhancing their potential applications, has been a key challenge. To date, only Zhao et al. have reported that incorporating Hg in PbHg3Ti4O12 under high pressure alters the À -site square coordination, leading to the evolution of a ferroelectric phase.6 Yet, the toxicity of Hg and Pb makes this compound unsuitable for catalysis and other practical applications.

This report aims to create piezoelectric properties in quadruple perovskites and showcases the utilization of the created piezoelectric polarization to facilitate charge transport for enhanced photocatalysis. We use CaCu3Ti4O12 (CCTO), a typical lead-free quadruple perovskite with a narrow bandgap (1.7 eV) synthesized at ambient pressure and composed of earth-abundant and nontoxic elements, as the prototype material. For the first time, we demonstrate that the piezoelectricity in the centrosymmetric CCTO quadruple perovskite can be successfully created through a cation defect engineering strategy involving high-temperature treatment to induce lattice Cu exsolution and Cu vacancy formation. The presence of a Cu vacancy disturbs the local centrosymmetric lattice structure mainly by relaxing the rotation of the TiO6 octahedron to form local inhomogeneity, thus resulting in strong polarization and piezoelectricity in CCTO, which are verified by comprehensive experimental observations and computational modeling results. Another important function of the Cu vacancy is to finely tune the catalytic properties of CCTO by negatively shifting the d-band center of CCTO, which is favorable for the two-electron oxygen reduction reaction. Leveraging the synergy between the created piezoelectricity

and the inherent semiconducting properties, defect‐manipulated CCTO can overcome its original drawback of high charge transfer resistance and achieve efficient charge separation and transfer. As a result, the lifetime of photo‐excitations in defective CCTO is enhanced by 2.5 times, leading to an enhanced piezo-photocatalytic performance for reactive oxygen species (ROS) production with a dramatic 3.86- and 31-fold improvement over individual piezocatalysis and photocatalysis, respectively. The results demonstrate the effective strategy of cation defect engineering to create piezoelectricity in quadruple perovskites, as confirmed by its utilization to boost photocatalysis. The appearance of piezoelectricity in quadruple perovskite oxides could enable many advanced applications in modern microelectronics.

RESULTS AND DISCUSSION

Material Design and Structural Characterization. The transition of quadruple perovskite to the piezoelectric/ ferroelectric state is frustrated by the excessive structural stability, which results from the constrained flexibility of tilted octahedra by square-planar-coordinated Cu2+. 6,15 Breaking this constraint to enable controllable manipulation of the octahedral rotation is essential for realizing piezoelectricity. To achieve this, we employed a thermally driven cation‐exsolution strategy to precisely control the Cu exsolution from the CCTO lattice and create Cu vacancies. This approach is sourced from the thermal instability of the CuO constituent in the pseudoternary CaO-CuO-TiO2 (i.e., CCTO) system at high temperatures.15,16 According to the Ellingham diagram (Figure S1) and phase diagram of CCTO (Figure S2),15 the phase stability of CCTO is influenced significantly by temperature and oxygen partial pressure variations. Notably, the oxygen chemical potential line corresponding to the decomposition of CCTO lies below that of CuO in the Ellingham diagram, creating a substantial window (shadow area) that allows the CuO in the pseudoternary system to dissociate first upon pyrolysis. This permits the selective exsolution of Cu from the CCTO lattice in the atmosphere at temperatures above 1000 °C. Given this, the stoichiometric CCTO precursors were intentionally treated at various temperatures (1000, 1060, 1100, and 1140 °C) to control the Cu exsolution process.

The crystal structures of the four CCTO samples sintered at different temperatures were comparatively studied. The powder X-ray diffraction patterns (XRD) in Figure 1c,d and the corresponding Rietveld refinements (Figure S3 and Table S1) confirm that CCTO samples were mainly crystallized as the A-site ordered quadruple perovskite oxides (AÀ 3B4O12) with centrosymmetric crystalline phases, including a major cubic phase (space group: Im$\bar{3}$) and a minor rhombohedral phase (space group: R$\bar{3}$). Increasing the treatment temperature of CCTO from 1000 to 1140 °C significantly impacts the phase evolution and lattice parameters. The lattice of the major phase initially shrank upon the increase of sintering temperature, as evidenced by the positive shifts of diffraction peaks (Figure 1d) and a gradual reduction of lattice parameters (Table S1) from 7.3954 Å (CCTO-1000) to 7.3950 Å (CCTO-1060) and 7.3948 Å (CCTO-1100). However, a further temperature increase prompts a distinct recovery of the lattice (7.3951 Å) in CCTO-1140. This phenomenon stems from the formation of cation vacancies induced by Cu exsolution and phase segregation, as illustrated shortly. The scanning electron microscopy (SEM) and energy-dispersive X‐ray spectroscopy (EDS) mapping images in Figure S4 exhibit a homogeneous distribution of Ca and Ti but the agglomeration of Cu and O, signifying the formation of a Cu- and O-rich impurity phase, which has been identified as monoclinic CuO (space group: C12/c1). These findings verify that Cu exsolution from the stoichiometric CCTO leads to the formation of the CuO impurity phase and the corresponding cation vacancies in the CCTO lattice, thus causing lattice shrinkage. Further refinement analysis confirms a general increment of segregated CuO quantity with the elevated pyrolysis

temperature, reaching the highest content of CuO (3.53 wt %) in CCTO-1140. This mirrors that high temperature favors the Cu exsolution from the CCTO lattice, consistent with the trend of gradually lowered oxygen chemical potential of CuO with increased temperature (Figure S1).15 Meanwhile, based on the lattice Cu occupancy from the refinement results, the Cu vacancy contents in samples sintered from low to high temperatures were determined to be 12.0, 16.0, 20.4, and 17.5% in atomic ratio, respectively. In principle, the highest concentration of Cu vacancy should be achieved in CCTO-1140 due to the maximum Cu leaching from the CCTO lattice and the substantial formation of CuO impurity. However, a notable discrepancy between the CuO content and Cu vacancy was noticed in CCTO-1140, which exhibited a relatively lower content of Cu vacancy (17.5%) compared to that in CCTO-1100 (20.4%). The reason is that the excessive Cu exsolution from CCTO-1140 induced the partial collapse of the perovskite lattice and gave rise to the TiO2 phase (2.32 wt %, Figures S3d and S4c,d). This leads to a reduction in the content of A-site cation vacancies, a similar phenomenon previously observed in A-site-deficient BaSrCoFe double perovskite.17,18

The phase structure of CCTO was further validated by high□resolution transmission electron microscopy (HR-TEM). The coexistence of phases is clearly evidenced by the fast Fourier transform (FFT) patterns and lattice spacing measurements (Figures S5 and S6). The cubic diffraction pattern along the [001] zone axis is highly symmetric, while the rhombohedral structure is characterized by the (300) facet. Additionally, the aforementioned lattice parameter changes in the cubic CCTO induced by Cu exsolution can be distinctly reflected by the d□space change of the (220) lattice fringe, which undergoes a gradual decrease from 0.269 Å (CCTO-1000) to 0.265 Å (CCTO-1100), followed by a sudden increase at 1140 °C (0.268 Å) (Figure S5). In particular, Cu vacancies were captured in the major cubic phase. In Figure 1e,f, the facet exposure of the cubic phase along the [−111] zone axis reveals an ordinal arrangement of Ca and Cu. This well-ordered arrangement is confirmed by the periodic alternation of the atom intensity profile along path 1 (Figure 1g), exhibiting stronger peak intensity of Ca2+ with a larger radius (100 pm) than Cu2+ with a smaller size (73 pm). Both cations are distributed with an even planar distance of 3.08 Å. Cu vacancies were clearly observed along path 2 and within the area marked by the white dotted circle in Figure 1e. The presence of Cu deficiency altered the originally ordered structure and the distance between Ca and Cu near the defect site. As measured from the intensity profile along path 2, the planar distance between two nearest Ca and Cu pairs around the defective site significantly reduces to 2.75 and 2.16 Å, respectively, while that between the nearest Cu and next□nearest Ca was stretched to 3.25 Å with diminishing impact further afield. Furthermore, the geometric phase analysis unveils a dense lattice strain field over the defective facet, characterized by the alternative distribution of tensile and compressive strains (Figure S7). These observations vividly reflect the formation of local inhomogeneities in CCTO arising from both Cu exsolution and the Cu vacancy. To gain an in-depth insight into the phase evolution and the associated thermodynamic stability change of the defective CCTO, density functional theory (DFT) computation was performed over four structural models with varying Cu vacancy contents (assumed to be 0.0, 16.7, 33.3, and 50.0%, respectively). The energy-favorable configurations are depicted in Figure S8. Consistent with the experimental observation of the lattice shrinkage due to the formation of cation defects, the computed lattices along the a and b axes of crystals decreased from 7.3638(8) to 7.1980(5) Å and 7.3638(8) to 7.2333(0) Å, respectively. The introduction of Cu vacancy resulted in a distinguishable Ti−O bond-length variation (ca. 0.1 Å) in TiO6 octahedra near the defect site, inducing the distortion of TiO6 units (Figure 1h). Meanwhile, a local geometric configuration change was observed, with the inclination between two TiO6 moieties around the Cu vacancy increased from 62.7° in the stoichiometric configuration to 69.7° in the defective one (vacancy content of 50.0%),

suggesting the controllable relaxation of the pristine confined TiO6 octahedron tilting. These alterations would drive the inherent polarization and promote the charge redistribution, thus yielding the desirable polarization and piezoelectric property, which will be discussed in detail shortly. In addition to the structural changes, the variation of the thermodynamic stability of CCTO is also unveiled. The compositional phase diagram analysis finds an approximate concave hull for the Ca−Ti− Cu−O system (Figure 1i) and the formation energy is going downhill with the increase of Cu vacancy content, from 0.0 to 33.3%, indicating that the generation of Cu vacancy is thermodynamically favorable. However, further increasing the vacancy in CCTO (from 33.3 to 50.0%) is energetically prohibited. This explains that the CCTO perovskite structure cannot be sustained stably, so the secondary impurity of TiO2 is easily segregated when the Cu-defect concentration is sufficiently high, in agreement with the observed behavior in the case of CCTO-1140.

The chemical state change caused by defects was investigated by X-ray photoelectron spectroscopy (XPS) and X-ray absorption spectra (XAS). Along with the Cu vacancy formation, the significant positive shift of Cu 2p spectra (Figure S9a) implies the gradual reduction of electron density around the Cu atoms, while Ti shows a minor change in its chemical state (Figure S9b). The notable changes in Cu 2p spectra can be attributed to the Cu exsolution-induced oxidation of the residual Cu in CCTO. Owing to Cu exsolution from the perovskite lattice, the cations in CCTO must increase their oxidation states to maintain the charge neutrality within the material. Considering the unoccupied 3d orbitals in Ti4+, its further oxidation is difficult, but Cu2+ can evolve into Cu3+ under specific conditions.19 As a result, CCTO-1100, having the highest Cu vacancy, exhibits substantial oxidation of the Cu species. Cu K-edge X-ray absorption near edge structure (XANES, Figure S10) spectra reveal distinctive pre-edges of CCTO at higher energy compared to the CuO reference, signifying the higher Cu valence state than 2+ in CCTO. Besides, in line with the XPS result, CCTO samples show the Cu vacancy-dependent shift in the pre-edges, further corroborating the Cu exsolution and the associated change in oxidation states.

Cation Vacancy-Induced Piezoelectricity. Piezoelectric force microscopy (PFM) was employed to probe the piezoelectric properties of the CCTO samples. Figures 2a, 2b, and S11 show the topography and corresponding piezoresponse of CCTO-1100. The displacement amplitude, piezopotential, and phase signals of the observed particles display distinct contrast to the silicon substrate. By applying a tip bias loop between −10 and +10 V, the localized displacement-bias curve exhibits a typical butterfly loop (Figure 2b) with a ∼180° polarization domain switching. These results collectively evidence the robust piezoelectric and ferroelectric properties in CCTO.20−22 For quantitative evaluation, the piezoelectric coefficient d33 of each sample underwent multiple measurements. The results of each measurement and the corresponding average d33 are given in Figure S12 and Table S2. As observed, CCTO-1100 exhibited the highest d33 value of 7.0 pC N−1 followed by CCTO-1140 (4.8 pC N−1) and CCTO-1060 (4.6 pC N−1), while CCTO□1000 gave the lowest value (1.8 pC N−1).

Typically, conventional displacive ferroelectrics/piezoelec□trics with spontaneous polarization are characterized by the movement of the correlated displacive ions from their originally symmetric locations (nonpolar) to asymmetric positions at certain defined temperatures (Curie temperature), thus resulting in a polar structure with ferroelectricity and piezoelectricity.23−25 A representative example is the ferroelec□tricity of tetragonal BaTiO3 that arises from the Ti off-center displacement.26 Nevertheless, in CCTO quadruple perovskite, because of the high rigidity of the BO6 octahedra framework constrained by the Cu square-coordination configuration, neither a ferroelectric phase transition nor an ion-shift-induced long-range order structural change of CCTO was observed in our

structural analysis, suggesting the possibility of other mechanisms for the anomalous piezoelectricity. Notably, in this study, a straightforward correlation between the piezo□electricity and Cu deficiency content is evident (Figure 2c). The d33 value is linearly enhanced with an increase in the Cu vacancy concentration. This strongly proves that the abnormal piezoelectricity in CCTO stems from the lattice Cu deficiency, given its notable effect in breaking or distorting the local crystal symmetry.

To gain deeper insights, a combined theoretical and experimental analysis was performed. DFT computations were first employed to unveil the underlying polarization in the defective CCTO. It is noteworthy that the dipole moment in the crystal is highly associated with the polarization and piezoelectricity. For cubic crystals, the maximum longitudinal piezoelectric modulus occurs in the family of directions.27 We computed the dipole moments along the [111] directions for four CCTO structures (with Cu vacancy contents of 0.0, 16.7, 33.3, and 50.0%. respectively). Intriguingly, the dipole moment increases with Cu vacancy. The computed values of these four samples from low to high Cu vacancy contents are 1.21, 1.54, 1.56, and 1.65 e*Å, respectively. This indicates that the built-in electric field (intrinsic polarization) along the direction of the CCTO crystals is improved by Cu vacancy. The Cu vacancy□enhanced polarization has also been experimentally manifeste using XAS. The O K-edge XANES spectra in Figure 2d provide the bonding information on O with its coordination cations.28 Two peaks indicated by an asterisk (*) reflect the transition from the core level of the O 1s to the unoccupied 2p states hybridized with a metal 3d orbital. Notably, the peak shift and broadening feature are indicative of the crystal field change in CCTO, a phenomenon associated with the structural symmetry breaking and polarization field.29 Unfortunately, analyzing the subtle changes of hybridization proves challenging in O K-edge spectra due to the presence of both π (t2g levels) and σ (eg levels) interactions within a narrow energy window. Alternatively, Ti L-edge XAS spectra resulting from the 2p-3d transition with distinct separation between t2g and eg peaks offer an ideal means to determine the specific changes. As shown in Figure 2e, the typical t2g-eg splitting (t2g: dxy, dxz, dyz; eg: d ; d d z x y 2 2 2) is presented in all CCTO samples. Beyond that, an obvious Cu vacancy-dependent splitting of the eg peak (denoted as eg' and eg”) in CCTO has been observed. It should be noted that this change can result from either the Ti3+ species or the secondary crystal field splitting (i.e., splitting of eg degenerate orbitals).30 However, given that the presence of Ti3+ could simultaneously cause distinct changes in the t2g state, we do not observe any extra feature in t2g, excluding the potential contribution from Ti3+. Besides, the presence of Ti3+ is impossible in defective CCTO since all the cations tend to be in the oxidized state as illustrated above. Moreover, the standard Ti4+ L-edge spectrum of paraelectric CaTiO3 has been provided for reference, where its L2,3-edge spectra display high symmetry without eg degenerate orbitals splitting. It is thus safe to ascribe the changes in the Ti L-edge spectra of CCTO, especially the eg peak broadening, to the secondary crystal field splitting resulting from the localized structural symmetry disruption and the induced polarization field (Figure 2f). More specifically, the Ti eg orbitals point directly toward the 2p orbitals of the coordination O atoms, making the eg band highly sensitive to the local environment.31 The creation of the Cu vacancy gave rise to the local lattice distortion and enhanced structural polarization, which in turn affects the local orbitals and electronic configuration. Consequently, CCTO with higher Cu vacancy and stronger polarization demonstrates more pronounced eg orbital splitting (d ; d d z x y 2 2 2) as reflected by the increased intensity of eg” in the Ti L3-edge. These results undoubtedly evidence the key role of the Cu vacancy in the enhanced polarization and piezoelectricity.

Raman spectroscopy was applied to further investigate the structural changes because of its sensitivity to specific atomic motions,32 which hopefully helps to elucidate how Cu vacancies contribute to

polarization. As shown in Figure 3a, three of eight Γ-point phonon active modes (2Ag + 2Eg + 4Fg) of the Im3̄phase were detected in the four defective CCTO samples. The distinct peaks centered at 440 and 510 cm−1 can be assigned to Ag symmetry corresponding to TiO6 rotation or tilting, while the one at 572 cm−1 represents the Fg mode being relevant to the anti-stretching of O−Ti−O.33 Importantly, a noteworthy impact of the Cu vacancy on both Fg and Ag modes was witnessed, wherein the increased Cu vacancy content resulted in the gradual inactivation of the two modes, as evidenced by a considerable attenuation of their scattering intensity. Typically, charge redistribution and Ti−O bond length vibration within TiO6 octahedra would induce a strong effect on Ti−O stretching frequency, i.e., Fg modes.34 Thus, the reduction of the Fg band in CCTO implies Ti off-center away from its symmetric position in TiO6, consistent with the DFT prediction, which might be a root cause for the polarization. On the other hand, the much stronger reduction intensity ratio of Fg to Ag(2), means that Cu vacancy mainly results in a substantially lowered rotation of TiO6 octahedra. This has also been corroborated by another salient feature of the progressive splitting of Ag peaks with Cu vacancy formation, which arises due to variations in atomic arrange□ments caused by the relaxed TiO6 rotation.35 As seen in Figure 3b, the atomic motion in Ag(1) and Ag(2) modes explains well the diminished rotation behavior of TiO6. Owing to the Cu exsolution and breaking of Cu−O bonds, the constraint for the pristine TiO6 rotation (Figure 3c), required to accommodate the square-coordinated Cu, has been removed. As a result, the original tilting of TiO6 is relaxed, and the apical oxygen atom near the Cu vacancy shifts away from its original position. Such a relaxation of TiO6 tilting also affects the adjacent two Ca atoms. The two nearest Ca atoms would concomitantly shift away from the Cu vacancy and move close to the next adjacent Cu sites, disrupting the local structural symmetry. This aligns well with the HR-TEM and DFT structural simulation results that show that local inhomogeneity forms around defective Cu sites. Furthermore, through the investigation of the velocity autocorrelation function (VACF) and vibrational density of states (VDOS), the Cu defect-induced relaxation of TiO6 octahedra tilting can be discerned. Noteworthy is that the smaller thermal fluctuation in VACF indicates a lowered rotation or a smaller tilting degree. Figure 3d obtained from ab initio molecular dynamics (AIMD) simulation at room temperature (300 K), clearly indicates that the presence of Cu vacancies greatly lowers the rotation degree of TiO6 octahedra, and the fluctuation range of VACF is reduced from 0.24 at Cu full occupancy to about 0.10 at a vacancy content of 50.0%. The VACF can be further converted into the VDOS via a Fourier transform (Figure 3e). The vibrational frequency of four different CCTO samples shifts to lower values with increasing Cu vacancies, and the corresponding intensity of VDOS is weakened. These results unambiguously demonstrate that the body-centered symmetric structure of the ideal unit cell is locally destroyed mainly because of the relaxed TiO6 octahedra tilting around Cu vacancy, giving rise to the polarization and piezoelectricity. The other potential causes for the abnormal piezoelectricity in CCTO, such as the ordered accumulation of lattice oxygen defects,36 have also been discussed and excluded as illustrated in Note S1 and Figures S13 and S14.

Application in Piezo-Photocatalysis. With the success□fully engineered piezoelectricity in CCTO, we then demonstrate the utilization of piezoelectricity to promote photo□catalysis through the systematic evaluation of the catalytic performance. Initially, we assessed the optical properties and band structure (Figures S15 and S16) of CCTO to ascertain their redox abilities. As depicted in Figure S17, the narrow band gap (∼1.7 eV) coupled with the appropriate band position enables a wide range of light absorption and offers the possibility to facilitate the oxygen reduction reaction (ORR). The results of catalytic ROS production are summarized in Figure 4a−c. In the absence of CCTO (blank experiment), the electron paramagnetic resonance (EPR) spectra of the reaction system show a negligible signal upon exposure to

light and ultrasonication. In contrast, with the presence of catalysts and external light and ultrasonic stimulation, substantial EPR signals of singlet oxygen (1 O2), superoxide radicals (O2 •−), and hydroxyl radicals (• OH) were detected, mirroring efficient ROS production via piezo-photocatalysis over CCTO. It is noteworthy that the intensities of the signal for 1 O2 and O2 •− are positively correlated to material piezoelectricity (specifically, CCTO-1100 > CCTO-1140 ≈ CCTO-1060 > CCTO-1000). This highlights the dominant role of piezoelectricity in the catalytic reaction. In addition, compared to the individual processes of piezocatalysis and photocatalysis, piezo-photocatalysis exhibits a considerable enhancement in the production of ROS (Figure 4d). This observation underscores a synergistic effect between the created piezoelectricity and photocatalysis. Consistent with the EPR results, the quantification of the generated H2O2 and radicals further substantiated the piezophotocatalytic activity of CCTO. The blank experiment displayed inert behavior, with no detectable product, while ROS were efficiently generated by CCTO. As shown in Figures 4e and S18, CCTO-1100 demonstrated a superior piezophotocatalytic performance among the four samples, delivering much higher concentrations of H2O2 (162 μM) and radicals (40 μM • OH and 22 μM • O2 −) within 2 h. In comparison, both CCTO-1060 and CCTO-1140 exhibited comparable but moderate catalytic activities, with the H2O2 concentration decreasing to 131 μM for CCTO-1060 and 121 μM for CCTO-1140. Meanwhile, the • O2 − and • OH yields for both samples were reduced to approximately 15 and 35 μM, respectively. CCTO-1000, with relatively weak piezoelectricity, showed a limited yield of H2O2 (64 μM), • O2 − (10 μM), and • OH (30 μM).

To evaluate the synergistic effect and identify the contributions of individual photocatalysis and piezocatalysis, control experiments were performed. As depicted in Figures 4f and S19, photocatalysis over CCTO exhibited minor H2O2 production attributed to the charge transfer resistance and sluggish carrier mobility (Figure S20), whereas piezocatalysis generated variable amounts of H2O2 depending on the sample's piezoelectricity, albeit much inferior to piezophotocatalysis. Taking CCTO-1100 as an example, the amount of H2O2 generated via piezo-photocatalysis was 3.86 and 31 times that from sole piezocatalysis and photocatalysis, respectively, demonstrating the strongest synergistic effect. As for the other ROS (radicals and 1 O2), it is hard to directly measure their synergistic effect owing to the difficulty in quantifying 1 O2. However, considering the highly oxidative nature of these oxygen species, the degradation of methylene blue (MB) was employed to assess the overall oxidation capacity of the reaction system, indirectly reflecting the radicals and 1 O2 productivity. The results, as detailed in Figure S21, reveal a similar piezoelectricity-dependent synergy. The stability of CCTO-1100 for MB degradation by oxidation was examined (Figure S22). After four consecutive runs of piezo-photocatalysis, the sample demonstrated sustained activity, maintaining performance comparable to the original value. In summary, these findings collectively verify that the defect-induced piezoelectricity in CCTO can effectively enhance photocatalysis for the production of ROS. The primary product, H2O2, along with diverse oxidative oxygen species, is efficiently generated via piezo-photocatalysis.

Mechanistic Study. Drawing insights from band structure analysis and catalytic results, we propose a reaction mechanism for oxygen reduction leading to ROS generation on CCTO. The validity of this reaction pathway was confirmed by the competition reactions using Ag+ , p-benzoquinone (p-BQ), and tert-butyl alcohol (t-BA) as scavengers for electrons, • O2 −, and • OH, respectively. In piezo-photocatalysis, Ag+ and p-BQ almost halted the H2O2 production, while t-BA had a negligible effect (Figure S23). Moreover, the reaction was severely inhibited in an N2-saturated solution. These results can infer that the generation of ROS stems from O2 activation. During this process, dissolved O2 molecules adsorbed on the catalyst surface (OO*) can be directly activated to produce 1 O2 and • O2 −,

37 which can also experience a further two-step reduction by excited electrons to form H_2O_2 ($O_2 + \bar{e} + H^+ \rightarrow OOH^*$, $OOH^* + \bar{e} + H^+ \rightarrow H_2O_2$) as evidenced by in situ Fourier-transform infrared spectroscopy (FT-IR) results (Figure 5a). However, since holes on the valence band can hardly oxidize water into • OH owing to the insufficient oxidation potential, it is inferred that • OH might be secondary products related to the H_2O_2 decomposition. This conjecture has been proven by H_2O_2 decomposition tests over CCTO catalysts (Figure S24), where all four catalysts exhibited moderate and similar abilities to decompose H_2O_2. This also rationalizes the observations that the • OH yields via piezo-photocatalysis over all samples are comparable and independent of their respective piezo-electricity.

DFT computations were further employed to track the transient intermediates and the reaction pathway. For two-electron ORR, the process is associated with the formation of adsorbed OOH* intermediates. The potential of photo-generated electrons (Ue) is defined as the energy difference between the zero potential and the conduction band minimum (CBM), which is estimated to be above 0.70 V for CCTO. First, we simulated the conditions in the absence of light irradiation (Ue = 0, Figure S25). It was found that the two-electron ORR is suppressed during the OOH* formation step ($O_2 + H^+ + e^- \rightarrow OOH^*$) on the surface of three defective CCTO catalysts. The potential barriers of ORR on these three CCTO samples were estimated to be 0.22, 0.57, and 0.67 eV, respectively. Whereas the protonation of OOH* into H_2O_2 ($OOH^* + H^+ + e^- \rightarrow H_2O_2$) is identified as the potential limiting step on the pristine perfect structure with an energy barrier of 0.29 eV. The above results indicate that the production of H_2O_2 via the ORR half-reaction on the CCTO surfaces is prohibited in the absence of light irradiation. Encouragingly, the elementary steps are shifted by Ue (Ue = 0.7 V) to include the external potential provided by photo-generated electrons. All the elementary steps along the two-electron ORR, including OOH* formation and OOH* protonation, become downhill in the free energy (Figure 5b). This suggests that CCTO is capable of catalyzing H_2O_2 production under light irradiation. However, because of the sluggish charge kinetics caused by the high electronic resistance of CCTO, the formed H_2O_2 is very limited via sole photocatalysis. In contrast, a large amount of H_2O_2 can be produced under simultaneous light and ultrasonication stimulation as aforementioned, highlighting the critical role of piezoelectric polarization in promoting the photocatalytic processes.38−40 Specifically, the built-in polarization field within CCTO can provide a long-range driving force to manipulate the bulk/surface electron and hole migration in opposite directions, thus improving the carrier separation and transport.40,41 The charge carrier dynamics of CCTO were investigated by using steady-state photoluminescence spec-troscopy (PL) and time-resolved PL (TR-PL). As shown in Figure 5c, the PL intensity arising from the radiative recombination of charge carriers was notably inhibited in CCTO with higher Cu defects, suggesting the promoted carrier separation efficiency by Cu vacancy. Meanwhile, TR-PL spectra and fitting results (Figure 5d and Table S3) show that the average radiation lifetimes of CCTO-1000, −1060, −1100, and −1140 are 6.9, 9.1, 17.0, and 6.3 ns, respectively. CCTO-1100 with the highest Cu vacancy shows notably prolonged carrier lifetime compared to CCTO-1000. Nevertheless, in conventional circumstances, lattice defects intrinsically cause scattering of photoexcitations, thereby impeding their transfer and exacerbating the reverse recombination.42 Here the contrary trend observed in CCTO can be ascribed to the defect-induced polarization, effectively prompting charge migration and overwhelming the adverse effect of Cu vacancies themselves. When the material is under ultrasonic vibration, the generated piezoelectric polarization could provide a much stronger driving force for the charge migration (Figure S26).38,43 These findings firmly confirm the critical role of the Cu vacancy and the induced polarization and piezo-electricity in promoting the photocatalytic process for ROS generation.

For efficient ROS production, the selectivity toward the two-electron process against the competitive four-electron ORR ($O_2 + 4\ H^+ /e^- \rightarrow H_2O$) is also crucial. Therefore, the electron transfer number and H_2O_2 selectivity of the ORR on CCTO were measured with a rotating ring-disk electrode (RRDE) in an O_2-saturated system. Figure 5e gives the linear sweep voltammetry (LSV) curves with the dioxygen reduction current measured on the disk electrode and the H_2O_2 oxidation current obtained on the Pt ring electrode. All CCTO compounds exhibited obvious H_2O_2 oxidation currents at a potential range below 0.7 V (vs RHE), suggesting notable catalytic activities toward H_2O_2 production. Importantly, the calculated electron transfer number and H_2O_2 selectivity show distinct dependence on the content of Cu vacancy (Figure 5e inset), where CCTO-1000 with the lowest concentration of Cu vacancy only gave rise to a H_2O_2 selectivity of ∼50% as a result of the joint two- and four-electron pathways. In stark contrast, CCTO-1100 with the most Cu defects showed a dominant two-electron pathway and an enhanced H_2O_2 selectivity of ∼80%, while moderate H_2O_2 selectivity was achieved on CCTO-1060 (70%) and CCTO-1140 (65%). The competitiveness between the two-electron and four-electron pathways was evaluated using the free energy difference between the H_2O_2 and O* ($\Delta G(*O) - \Delta G(H_2O_2)$), a descriptor reported previously.44 According to the definition, a more positive value of $\Delta G(O^*) - \Delta G(H_2O_2)$ (>0 eV) indicates a stronger preference for 2-electron ORR and selective ROS production.45 The calculated values of $\Delta G(O^*) - \Delta G(H_2O_2)$ on the four CCTO samples (i.e., CCTO with Cu vacancy content of 0.0%, 16.7%, 33.3%, and 50.0%) are 0.08, 0.04, 0.69, and 0.81 eV, respectively, which implies that the formation of Cu vacancy can greatly enhance the selectivity for a two-electron ORR, agreeing well with the experimental observation.

To reveal the underlying electronic origin associated with the intermediate adsorption difference, the density of states (DOS) of these four materials (surface states of active Cu sites shown in Figure 5f) was computed. In general, the formation of the cation vacancy can significantly affect the distribution of Cu-3d electrons. With the increased vacancy content, the CCTO tends to shift the d-electrons to more negative energy levels. The d-band center, a good indicator to assess the relative position of d-electrons, is decreased from −1.58 eV at a vacancy content of 0.0% to −3.10 eV at 50.0%. Notably, a more negative value of the d-band center would result in a weak binding with adsorbates.46 Therefore, the adsorption strength of the key intermediates (OOH* and O*) was reduced, preventing further deep reduction (four-electron ORR). These results prove that Cu vacancy can tailor the material's electronic configuration to promote the ORR from the four-electron pathway toward the two-eletron pathway.

Summarizing the above catalytic activity analysis with selectivity evaluation, it is concluded that the introduction of Cu vacancies in CCTO serves two key roles: (i) creating polarization and piezoelectricity within CCTO to improve photogenerated charge dynamics in photocatalysis; (ii) simultaneously tailoring the activity and selectivity by negatively shifting the energy levels of Cu-3d electrons, thereby weakening the interactions with OOH*/O*. As a result, the combined ultrasonic and light irradiation strategy shows enhanced performance toward ROS production.

CONCLUSIONS

The intrinsic crystallographic symmetry and the frustrated phase transition in cation-ordered structures have remained major obstacles to unlocking piezoelectricity in quadruple perovskites. We circumvented this limitation and successfully demonstrated piezoelectricity in centrosymmetric quadruple perovskite oxides via cation defect engineering. The precise control of Cu nonstoichiometry, through a facile thermal-driven cation exsolution method, effectively destabilizes the rigid BO_6 octahedra framework

and manipulates octahedral rotation, giving rise to local structural inhomogeneity and robust piezoelectric properties. This strategy, by utilizing cation defects, not only provides a viable pathway for creating piezoelectricity in quadruple perovskites to expand their potential applications but also facilitates the design of novel piezoelectric materials from those environmentally friendly centrosymmetric compounds. Additionally, our findings reveal a tunable d-band electronic configuration in CCTO materials by controlling Cu cation vacancy concentration, further highlighting the versatility of cation defects in optimizing catalytic properties. Consequently, we demonstrate the application of the engineered piezoelectricity and optimized electronic structure in CCTO to promote photocatalysis, enabling a 2.5-fold increment in the lifetime of photo□excitations and high selectivity toward hydrogen peroxide. This advancement will broaden the range of available candidates beyond noncentrosymmetric materials for piezoca□talysis and piezo-photocatalysis, offering possibilities for efficient energy conversion systems.

EXPERIMENTAL SECTION

Preparation of $CaCu_3Ti_4O_{12}$ Quadruple Perovskite Oxides. A sol−gel method employing citric acid (CA) as the complexing agent was adopted for the preparation of $CaCu_3Ti_4O_{12}$ (CCTO) quadruple perovskite oxides. Typically, 6.8064 g of titanium butoxide was dissolved in 20 mL of absolute ethanol (solution A) with continuous magnetic stirring at room temperature. Concurrently, stoichiometric amounts of calcium and copper nitrates were dissolved in 10 mL of ultrapure water to form solution B. CA (16.8112 g) was then introduced to solution A, followed by stirring at 50 °C for 2 h. Solution B was slowly added to solution A, and the final mixture was evaporated at 80 °C to remove excess ethanol and water until a transparent gel was obtained. This gel was sintered in an oven at 250 °C for 5 h to obtain the powder precursor. The final calcination was conducted at 1000, 1060, 1100, and 1140 °C for 10 h at a heating rate of 5 °C/min to produce the desired catalysts. These four samples were denoted as CCTO-1000, CCTO-1060, CCTO-1100, and CCTO-1140. The disk samples of the four CCTO catalysts were fabricated by pressing pretreated powder precursors (800 °C for 4 h) at 30 MPa for 20 min. This was followed by the same calcination procedure as previously mentioned.

Characterization. X-ray diffraction was performed on a Rigaku Ultima IV diffractometer in the range of 10° to 90° (2θ) with a slow scan rate of 2° per minute to analyze the crystalline structures. Rietveld refinement analysis was performed with Topas software to confirm the lattice parameters and phase structure. The structure and morphology of the prepared catalysts were characterized by transmission electron microscopy (TEM, Titan, FEI) and field emission scanning electron microscopy (SEM, Zeiss Neon 40EsB FIBSEM). X-ray photoelectron spectra (XPS) and ultraviolet photoelectron spectra (UPS) were recorded using a Thermo ESCALAB 250XI spectrometer with an Al−Kα X-ray gun. UV−vis diffuse reflection spectroscopy (DRS) of the samples was collected on a Shimadzu UV3600. Raman spectra were obtained on a LabRAM HR evolution spectrophotometer (532 nm excitation). Piezoelectric properties were examined by an atomic force microscope (AFM, Dimension Icon 11 Bruker) equipped with a piezoresponse force microscope (PFM) system, and the piezoelectric constant d33 was measured on a ZJ-3A d33 testing facility. PL spectra and time-resolved PL spectra were collected on a fluorescence spectrophotometer (FLSP-900, Edinburgh Instruments). Electrochemical tests were performed on an electrochemical working station (CHI760E). The rotating ring-disk electrode (RRDE, PINE Research) was used to determine the catalyst selectivity toward the 2-electron oxygen reduction reaction. The X-ray absorption spectra (XAS) measure□ments were conducted at the Australian Synchrotron (ANSTO), Victoria.

Catalytic Activity Evaluation. Catalytic oxygen reduction reactions (ORR) were conducted in a glass reactor (200 mL) under light and/or ultrasonic irradiation according to different reactions. The light and ultrasonic sources were provided by a Xenon lamp (300 W, λ > 420 nm) (Perfect Light, Beijing) and an ultrasonic generator (180 W, 40 kHz), respectively. Tap water (∼20 °C) was used as the circulating water to maintain the reaction temperature. The catalytic product yields were monitored with chemical probes. Specifically, for hydrogen peroxide, the reaction system containing dispersed catalysts (50 mg) and the mixture solution of DI water (45 mL) and absolute ethanol (5 mL) was irradiated by light and/or ultrasonic to start the reaction. At certain time intervals, 3 mL of the mixture was withdrawn and centrifuged at 13000 rpm for 15 min to remove the catalysts. Then 0.5 mL of the suspension was mixed with prepared KI solution (2 mL, 0.1 M) and ammonium molybdate solution (50 μL, 0.01 M) for reacting 10 min; the absorbance of which was detected by using a UV−vis spectrometer (725N, INESA) at the wavelength of 352 nm to determine the H2O2 concentration.47 The yields of hydroxyl radicals (• OH) and superoxide radicals (• O2̄) were quantified by terephthalic acid photoluminescence (TA-PL) and Nitroblue tetrazolium (NBT) transformation methods, respectively.48 For this purpose, catalysts (50 mg) were added into 50 mL of an NBT (0.025 mM) or TA (0.5 mM) solution for catalytic reaction. As NBT exhibits the maximum absorption at 259 nm and can be reduced by • O2 − in a molar ratio of 1:4, the amount of generated • O2 − was monitored by measuring the reduction of NBT. TA could react with • OH to produce 2- hydroxyterephthalic acid (2H-TPA) with a fluorescence emission at 452 nm. Therefore, the quantification of • OH can be achieved by observing the fluorescence intensity of 2H-TPA at 452 nm with an excitation wavelength of 315 nm in the reaction solution.

Methylene blue (MB, 10 ppm) oxidation experiments via sole piezo/photocatalysis or piezo-photocatalysis were performed using the same conditions and setup as aforementioned to evaluate the oxidative capability of each system. The MB concentration during the degradation process was measured by a UV−vis spectrometer at 664 nm. The degradation rate was determined by calculating the ratio of the residual concentration to the concentration after initial adsorption balance (C/C0).

Computational Methods. All the computations were carried out using the spin-polarized DFT method as implemented in the Vienna Ab initio Simulation Package (VASP).49 The Perdew−Burke− Ernzerhof (PBE) functional within the generalized gradient approximation (GGA) was employed to model the exchange□correlation energy. A plane-wave cutoff energy of 400 eV and dipole corrections were adopted for all of the computations. The long-range dispersion was corrected by the DFT+D3 method of Grimme.50 The Brillouin zone was sampled by 0.06 π/Å k-points using the Gamma scheme. The energy and force convergence thresholds for the iteration in the self-consistent field (SCF) were set to 10−5 eV and 0.02 eV/Å, respectively. The formation energy of the material was computed by the equation o f = [x] x E E (3) 4 12 /(20) F CaCu3 xTi 4O12 Ca Cu Ti O , where ECaCu3 xTi 4O12 is the total energy of ECaCu3 xTi 4O12 , and μCa, μCu, μTi, and μ0 are the chemical potentials of Ca, Cu, Ti, and O, respectively, which are referred to as the energy per atom of their bulk phases. The free energy diagrams of the oxygen reduction reaction on the (111) surfaces were obtained based on the computational hydrogen electrode (CHE) model proposed by Nørskov et al.51 To prevent artificial interactions between periodic images, a vacuum space of at least 12 Å was applied in the perpendicular direction of the slab surface.

REFERENCES

(1) Lu, Y.; Huang, Y.; Xu, Z.; Yang, K.; Bao, W.; Lu, Q. Quantifying Electrochemical Driving Force for Exsolution in Perovskite Oxides by Designing Graded Oxygen Chemical Potential. ACS Nano 2023, 17, 14005−14013.

(2) Zhuo, F.; Zhou, X.; Gao, S.; Höfling, M.; Dietrich, F.; Groszewicz, P. B.; Fulanovic, L.; Breckner, P.; Wohninsland, A.; Xu, B.-X.; Kleebe, H. J.; Tan, X.; Koruza, J.; Damjanovic, D.; Rodel, J. Anisotropic Dislocation-Domain Wall Interactions in Ferroelectrics. Nat. Commun. 2022, 13 (1), 6676.

(3) Zheng, H.; Liu, Y.; Ma, Z.; Debroye, E.; Ye, J.; Zhang, L.; Liu, T. High-Entropy Perovskite Oxides as a Family of Electrocatalysts for Efficient and Selective Nitrogen Oxidation. ACS Nano 2024, 18, 17642−17650.

(4) Chen, W.-T.; Mizumaki, M.; Seki, H.; Senn, M. S.; Saito, T.; Kan, D.; Attfield, J. P.; Shimakawa, Y. A Half-Metallic A- and B-Site Ordered Quadruple Perovskite Oxide CaCu3Fe2Re2O12 with Large Magnetization and a High Transition Temperature. Nat. Commun. 2014, 5, 3909.

(5) Etani, H.; Yamada, I.; Ohgushi, K.; Hayashi, N.; Kusano, Y.; Mizumaki, M.; Kim, J.; Tsuji, N.; Takahashi, R.; Nishiyama, N.; Inoue, T.; Takano, M. Suppression of Intersite Charge Transfer in Charge-Disproportionated Perovskite YCu3Fe4O12. J. Am. Chem. Soc. 2013, 135 (16), 6100−6106.

(6) Zhao, J.; Gao, J.; Li, W.; Qian, Y.; Shen, X.; Wang, X.; Shen, X.; Hu, Z.; Dong, C.; Huang, Q.; Cao, L.; Li, Z.; Zhang, J.; Ren, C.; Duan, L.; Liu, Q.; Yu, R.; Ren, Y.; Weng, S. C.; Lin, H. J.; et al. A Combinatory Ferroelectric Compound Bridging Simple ABO3 and A Site-Ordered Quadruple Perovskite. Nat. Commun. 2021, 12 (1), 747.

(7) Shimakawa, Y. A-Site-Ordered Perovskites with Intriguing Physical Properties. Inorg. Chem. 2008, 47, 8562−8570.

(8) Long, Y. W.; Hayashi, N.; Saito, T.; Azuma, M.; Muranaka, S.; Shimakawa, Y. Temperature-Induced A−B Intersite Charge Transfer in an A-Site-ordered LaCu3Fe4O12 Perovskite. Nature 2009, 458, 60− 63.

(9) Yamada, I.; Marukawa, S.; Murakami, M.; Mori, S. True" Negative Thermal Expansion in Mn-Doped LaCu3Fe4O12 Perovskite Oxides. Appl. Phys. Lett. 2014, 105, 231906.

(10) Hailili, R.; Wang, Z.-Q.; Li, Y.; Wang, Y.; Sharma, V. K.; Gong, X.-Q.; Wang, C. Oxygen Vacancies Induced Visible-Light Photocatalytic Activities of CaCu3Ti4O12 with Controllable Morphologies for Antibiotic Degradation. Appl. Catal., B 2018, 221, 422−432.

(11) Hu, C.; Tu, S.; Tian, N.; Ma, T.; Zhang, Y.; Huang, H. Photocatalysis Enhanced by External Fields. Angew. Chem., Int. Ed. 2021, 60, 16309−16328.

(12) Guo, S.-L.; Lai, S.-N.; Wu, J. M. Strain-Induced Ferroelectric Heterostructure Catalysts of Hydrogen Production through Piezophototronic and Piezoelectrocatalytic System. ACS Nano 2021, 15, 16106−16117.

(13) Liu, Q.; Zhan, F.; Luo, H.; Luo, X.; Yi, Q.; Sun, Q.; Xiao, Z.; Zhang, Y.; Zhang, D.; Bowen, C. R. Na-Sm Bimetallic Regulation and Band Structure Engineering in CaBi2Nb2O9 to Enhance Piezo-PhotoCatalytic Performance. Adv. Funct. Mater. 2023, 33 (38), 2303736.

(14) Ye, X.; Song, S.; Li, L.; Chang, Y. C.; Qin, S.; Liu, Z.; Huang, Y. C.; Zhou, J.; Zhang, L. J.; Dong, C. L.; Pao, C. W.; Lin, H. J.; Chen, C. T.; Hu, Z.; Wang, J. Q.; Long, Y. A'−B Intersite Cooperation□Enhanced Water Splitting in Quadruple Perovskite Oxide Ca□Cu3Ir4O12. Chem. Mater. 2021, 33, 9295−9305.

(15) Jacob, K. T.; Shekhar, C.; Li, X.; Kale, G. M. Gibbs Energy of Formation of CaCu3Ti4O12 and Phase Relations in the System CaO− CuO/Cu2O−TiO2. Acta Mater. 2008, 56, 4798−4803.

(16) Adams, T. B.; Sinclair, D. C.; West, A. R. Decomposition Reactions in CaCu3Ti4O12 Ceramics. J. Am. Ceram. Soc. 2006, 89, 2833−2838.

(17) Ge, L.; Zhou, W.; Ran, R.; Liu, S.; Shao, Z.; Jin, W.; Xu, N. Properties and Performance o f A-Site Deficient (Ba0.5Sr0.5)1−xCo0.8Fe0.2O3−δ for Oxygen Permeating Membrane. J. Membr. Sci. 2007, 306, 318−328.

(18) Ge, L.; Ran, R.; Zhang, K.; Liu, S.; Shao, Z. Oxygen Selective Membranes Based on B-site Cation-Deficient (Ba0.5Sr0.5)- (Co0.8Fe0.2)yO3−δ Perovskite with Improved Operational Stability. J. Membr. Sci. 2008, 318, 182−190.

(19) Harris, D. C.; Hewston, T. A. Determination of Cu3+/Cu2+ Ratio in the Superconductor YBa2Cu3O8−x. J. Solid State Chem. 1987, 69, 182−185.

(20) Wang, Y.; Wen, X.; Jia, Y.; Huang, M.; Wang, F.; Zhang, X.; Bai, Y.; Yuan, G.; Wang, Y. Piezo-Catalysis for Nondestructive Tooth Whitening. Nat. Commun. 2020, 11 (1), 1328.

(21) Ma, J.; Xiong, X.; Wu, D.; Wang, Y.; Ban, C.; Feng, Y.; Meng, J.; Gao, X.; Dai, J.-Y.; Han, G.; Gan, L.-Y.; Zhou, X. Band Position□Independent Piezo-Electrocatalysis for Ultrahigh CO2 Conversion. Adv. Mater. 2023, 35 (21), 2300027.

(22) Tian, W.; Han, J.; Wan, L.; Li, N.; Chen, D.; Xu, Q.; Li, H.; Lu, J. Enhanced Piezocatalytic Activity in Ion-Doped SnS2 via Lattice Distortion Engineering for BPA Degradation and Hydrogen production. Nano Energy 2023, 107, 108165.

(23) Su, R.; Wang, Z.; Zhu, L.; Pan, Y.; Zhang, D.; Wen, H.; Luo, Z.- D.; Li, L.; Li, F.-T.; Wu, M.; He, L.; Sharma, P.; Seidel, J. Strain Engineered Nano-Ferroelectrics for High-Efficiency Piezocatalytic Overall Water Splitting. Angew. Chem., Int. Ed 2021, 60, 16019− 16026.

(24) Liu, Y.; Withers, R. L.; Wei, X. Y. Structurally Frustrated Relaxor Ferroelectric Behavior in CaCu3Ti4O12. Phys. Rev. B 2005, 72, 134104.

(25) Ni, L.; Chen, X. M.; Liu, X. Q.; Hou, R. Z. Microstructure□Dependent Giant Dielectric Response in CaCu3Ti4O12 Ceramics. Solid State Commun. 2006, 139, 45−50.

(26) Zhu, P.; Chen, Y.; Shi, J. Piezocatalytic Tumor Therapy by Ultrasound-Triggered and BaTiO3-Mediated Piezoelectricity. Adv. Mater. 2020, 32 (29), 2001976.

(27) de Jong, M.; Chen, W.; Geerlings, H.; Asta, M.; Persson, K. A. A Database to Enable Discovery and Design of Piezoelectric Materials. Sci. Data 2015, 2 (1), 150053.

(28) Frati, F.; Hunault, M. O. J. Y.; de Groot, F. M. F. Oxygen K□edge X-Ray Absorption Spectra. Chem. Rev. 2020, 120, 4056−4110.

(29) Susarla, S.; García-Fernández, P.; Ophus, C.; Das, S.; Aguado□Puente, P.; McCarter, M.; Ercius, P.; Martin, L. W.; Ramesh, R.; Junquera, J. Atomic Scale Crystal Field Mapping of Polar Vortices in Oxide Superlattices. Nat. Commun. 2021, 12 (1), 6273.

(30) Stoyanov, E.; Langenhorst, F.; Steinle-Neumann, G. The Effect of Valence State and Site Geometry on Ti L3,2 and O K Electron Energy-Loss Spectra of TixOy Phases. Am. Mineral 2007, 92, 577− 586.

(31) Chen, S. C.; Sung, K. Y.; Tzeng, W. Y.; Wu, K. H.; Juang, J. Y.; Uen, T. M.; Luo, C. W.; Lin, J. Y.; Kobayashi, T.; Kuo, H. C. Microstructure and Magnetic Properties of Oxidized Titanium Nitride Thin Films In Situ Grown by Pulsed Laser Deposition. J. Phys. D: appl. Phys. 2013, 46, 075002.

(32) Du, Y.; Lu, T.; Li, X.; Liu, Y.; Sun, W.; Zhang, S.; Cheng, Z. High-Efficient Piezocatalytic Hydrogen Evolution by Centrosymmet□ric Bi2Fe4O9 Nanoplates. Nano Energy 2022, 104, 107919.

(33) Kolev, N.; Bontchev, R. P.; Jacobson, A. J.; Popov, V. N.; Hadjiev, V. G.; Litvinchuk, A. P.; Iliev, M. N. Raman spectroscopy of CaCu3Ti4O12. Phys. Rev. B 2002, 66, 132102.

(34) Espinoza-González, R.; Mosquera, E. Influence of Micro- and Nanoparticles of Zirconium Oxides on the Dielectric Properties of CaCu3Ti4O12. Ceram. Int. 2017, 43, 14659−14665.

(35) Litvinchuk, A. P.; Chen, C. L.; Kolev, N.; Popov, V. N.; Hadjiev, V. G.; Iliev, M. N.; Bontchev, R. P.; Jacobson, A. J. Optical Properties of High-Dielectric-Constant CaCu3Ti4O12 Films. Phys. Status Solidi. 2003, 195, 453−458.

(36) Park, D. S.; Hadad, M.; Riemer, L. M.; Ignatans, R.; Spirito, D.; Esposito, V.; Tileli, V.; Gauquelin, N.; Chezganov, D.; Jannis, D.; Verbeeck, J.; Gorfman, S.; Pryds, N.; Muralt, P.; Damjanovic, D. Induced Giant Piezoelectricity in Centrosymmetric Oxides. Science 2022, 375, 653−657.

(37) Wang, Y.; Xu, Y.; Dong, S.; Wang, P.; Chen, W.; Lu, Z.; Ye, D.; Pan, B.; Wu, D.; Vecitis, C. D.; Gao, G. Ultrasonic Activation of Inert Poly(tetrafluoroethylene) Enables Piezocatalytic Generation of Reactive Oxygen Species. Nat. Commun. 2021, 12 (1), 3508.

(38) Zhang, Y.; Phuong, P. T. T.; Roake, E.; Khanbareh, H.; Wang, Y.; Dunn, S.; Bowen, C. Thermal Energy Harvesting Using Pyroelectric-Electrochemical Coupling in Ferroelectric Materials. Joule 2

020, 4, 301−309.

(39) Amdouni, W.; Fricaudet, M.; Otonicar, M.; Garcia, V.; Fusil, S.; Kreisel, J.; Maghraoui-Meherzi, H.; Dkhil, B. BiFeO3 Nanoparticles: The “Holy-Grail” of Piezo-Photocatalysts? Adv. Mater. 2023, 35 (31), 2301841.

(40) Wang, K.; Han, C.; Li, J.; Qiu, J.; Sunarso, J.; Liu, S. The Mechanism of Piezocatalysis: Energy Band Theory or Screening Charge Effect? Angew. Chem., Int. Ed. 2022, 61 (6), No. e202110429.

(41) Chen, F.; Huang, H.; Guo, L.; Zhang, Y.; Ma, T. The Role of Polarization in Photocatalysis. Angew. Chem., Int. Ed. 2019, 58, 10061−10073.

(42) Sung, J.; Schnedermann, C.; Ni, L.; Sadhanala, A.; Chen, R. Y. S.; Cho, C.; Priest, L.; Lim, J. M.; Kim, H.-K.; Monserrat, B.; Kukura, P.; Rao, A. Long-Range Ballistic Propagation of Carriers in Methylammonium Lead Iodide Perovskite Thin Films. Nat. Phys. 2020, 16, 171−176.

(43) Hu, C.; Hu, J.; Zhu, Z.; Lu, Y.; Chu, S.; Ma, T.; Zhang, Y.; Huang, H. Orthogonal Charge Transfer by Precise Positioning of Silver Single Atoms and Clusters on Carbon Nitride for Efficient Piezocatalytic Pure Water Splitting. Angew. Chem., Int. Ed. 2022, 61 (43), No. e202212397.

(44) Guo, X.; Lin, S.; Gu, J.; Zhang, S.; Chen, Z.; Huang, S. Simultaneously Achieving High Activity and Selectivity toward Two Electron O2 Electroreduction: The Power of Single-Atom Catalysts. ACS Catal. 2019, 9, 11042−11054.

(45) Mok, D. H.; Back, S.; Siahrostami, S. Validating ΔΔG Selectivity Descriptor for Electrosynthesis of H2O2 from Oxygen Reduction Reaction. Angew. Chem., Int. Ed. 2024, 63 (23), No. e202404677.

(46) Wang, Z.; Huang, J.; Wang, L.; Liu, Y.; Liu, W.; Zhao, S.; Liu, Z.-Q. Cation-Tuning Induced d-Band Center Modulation on CoBased Spinel Oxide for Oxygen Reduction/Evolution Reaction. Angew. Chem., Int. Ed. 2022, 61 (16), No. e202114696.

(47) Hu, C.; Huang, H.; Chen, F.; Zhang, Y.; Yu, H.; Ma, T. Coupling Piezocatalysis and Photocatalysis in Bi4NbO8X (X = Cl, Br) Polar Single Crystals. Adv. Funct. Mater. 2020, 30 (7), 1908168.

(48) Wang, P.; Li, X.; Fan, S.; Chen, X.; Qin, M.; Long, D.; Tadé, M. O.; Liu, S. Impact of Oxygen Vacancy Occupancy on Piezo-Catalytic Activity of BaTiO3 nanobelt. Appl. Catal., B 2020, 279, 119340.

(49) Blöchl, P. E. Projector Augmented-Wave Method. Phys. Rev. B 1994, 50, 17953−17979.

(50) Grimme, S. Semiempirical GGA-Type Density Functional Constructed with a Long-Range Dispersion Correction. J. Comput. Chem. 2006, 27, 1787−1799.

(51) Nørskov, J. K.; Rossmeisl, J.; Logadottir, A.; Lindqvist, L.; Kitchin, J. R.; Bligaard, T.; Jónsson, H. Origin of the Overpotential for Oxygen Reduction at a Fuel-Cell Cathode. J. Phys. Chem. B 2004, 108, 17886−17892.

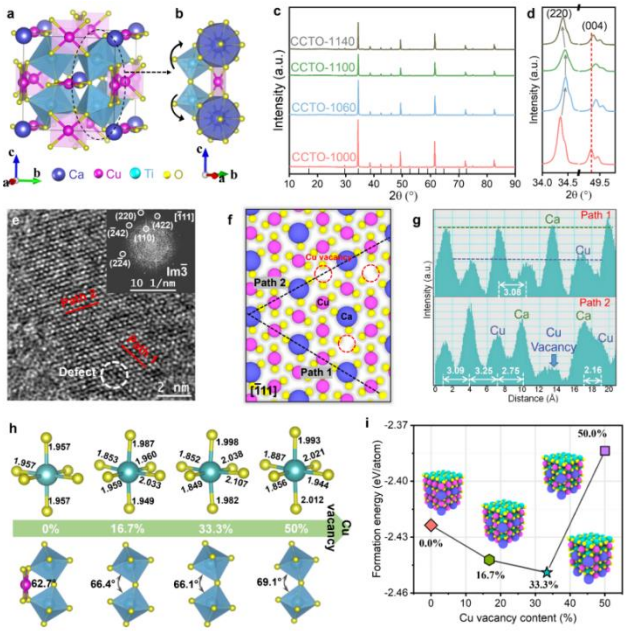


Figure 1. Structural characterizations of CCTO: (a) schematic illustration of the cubic crystal structure (space group: Im3̄) of CCTO quadruple perovskite; (b) schematic illustration of the A-site Ca coordination and TiO6 octahedra tilting; (c) XRD patterns of CCTO; (d) enlarged XRD; (e) HR-TEM image of Im3̄phase, and (f) the corresponding atom arrangement along the zone axis; (g) the corresponding intensity profiles along paths 1 and 2; (h) theoretical simulation of TiO6 octahedra distortion (top) and tilting change (bottom) around the Cu vacancy; (i) the calculated formation energy of the CCTO system with varied Cu vacancy content.

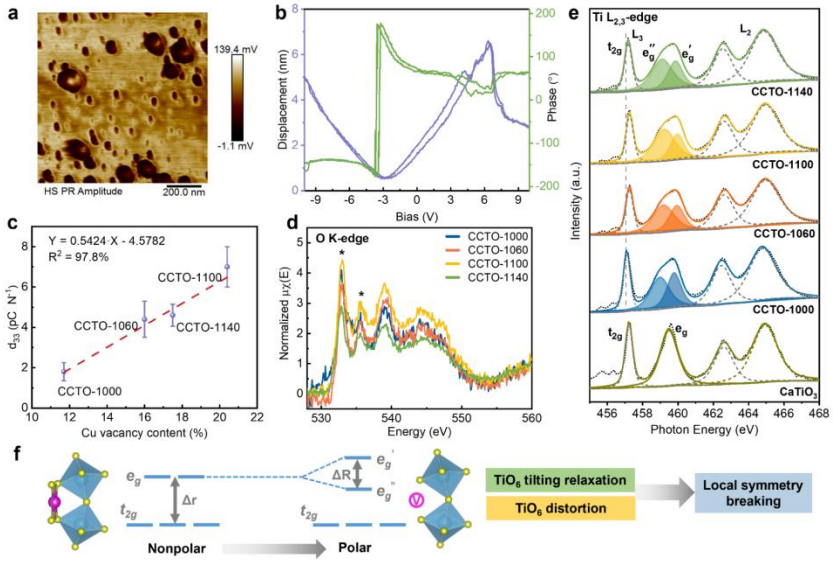


Figure 2. Piezoelectric properties and electronic structures of defective CCTO. (a) Piezopotential map; (b) the localized displacement− voltage curve and phase reversion profile of CCTO-1100; (c) the linear correlation between the content of Cu vacancy and piezoelectric constant d33; (d) O K-edge XAS of CCTO; (e) Ti L-edge XAS of CCTO; (f) schematic illustration of crystal field splitting in defective CCTO.

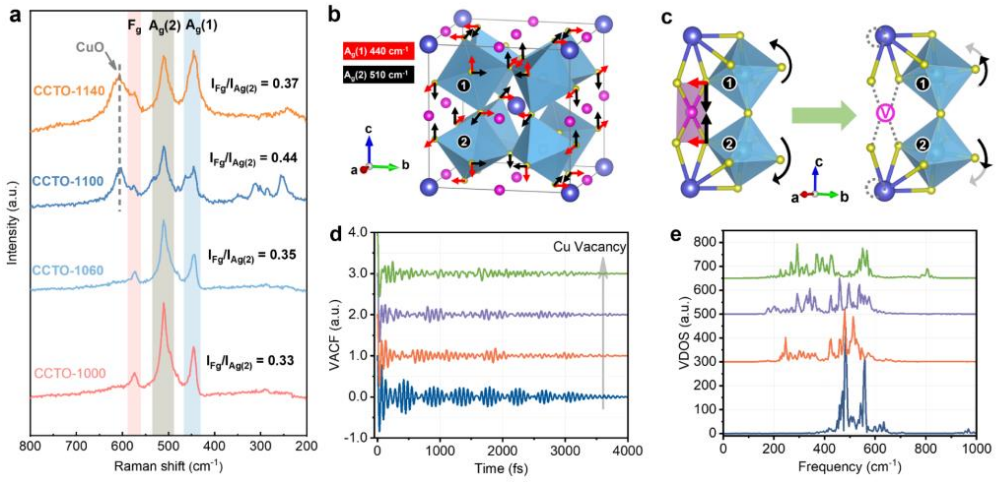


Figure 3. Origin of piezoelectricity in defective CCTO. (a) Raman spectra of CCTO; (b) atomic motion in the Ag(1) mode (red arrows) and Ag(2) mode (black arrows); (c) schematic illustration of TiO6 tilting relaxation and atomic movements around the defective site; (d) profiles of the velocity autocorrelation function (VACF), and (e) the corresponding vibrational density of states (VDOS) of CCTO.

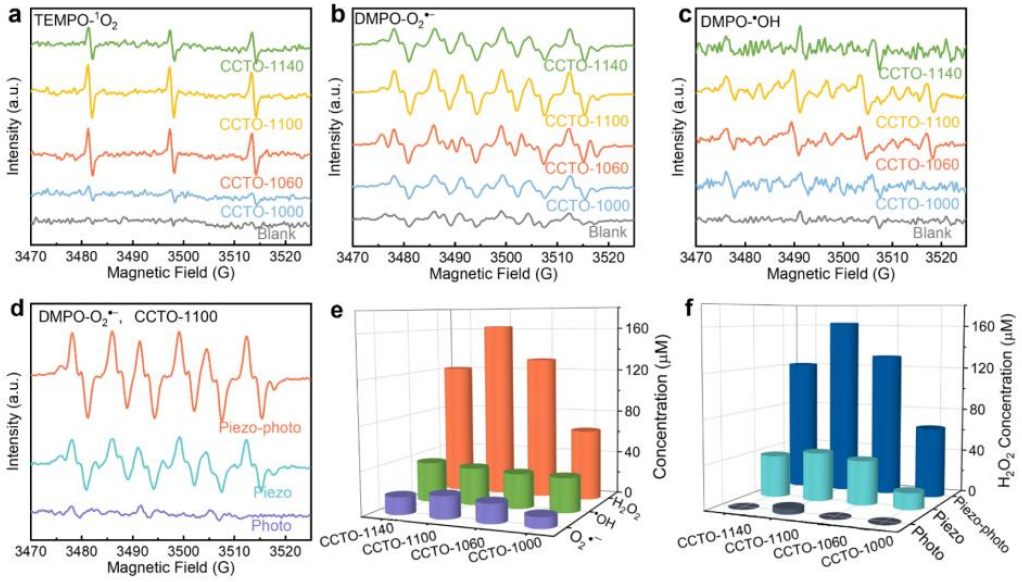


Figure 4. Piezo-photocatalytic performance of CCTO samples. EPR spectra of (a) TEMPO-1 O2, (b) DMPO-O2 •−, and (c) DMPO-• OH by piezo-photocatalysis over four CCTO samples; (d) EPR spectra of DMPO-O2 •− over CCTO-1100 by photocatalysis, piezocatalysis, and piezo-photocatalysis, respectively; (e) the concentrations of piezo-photocatalytically generated H2O2, O2 •−, and • OH over four CCTO samples at 2 h; (f) H2O2 concentration generated via piezocatalysis, photocatalysis, and piezo-photocatalysis after 2 h.

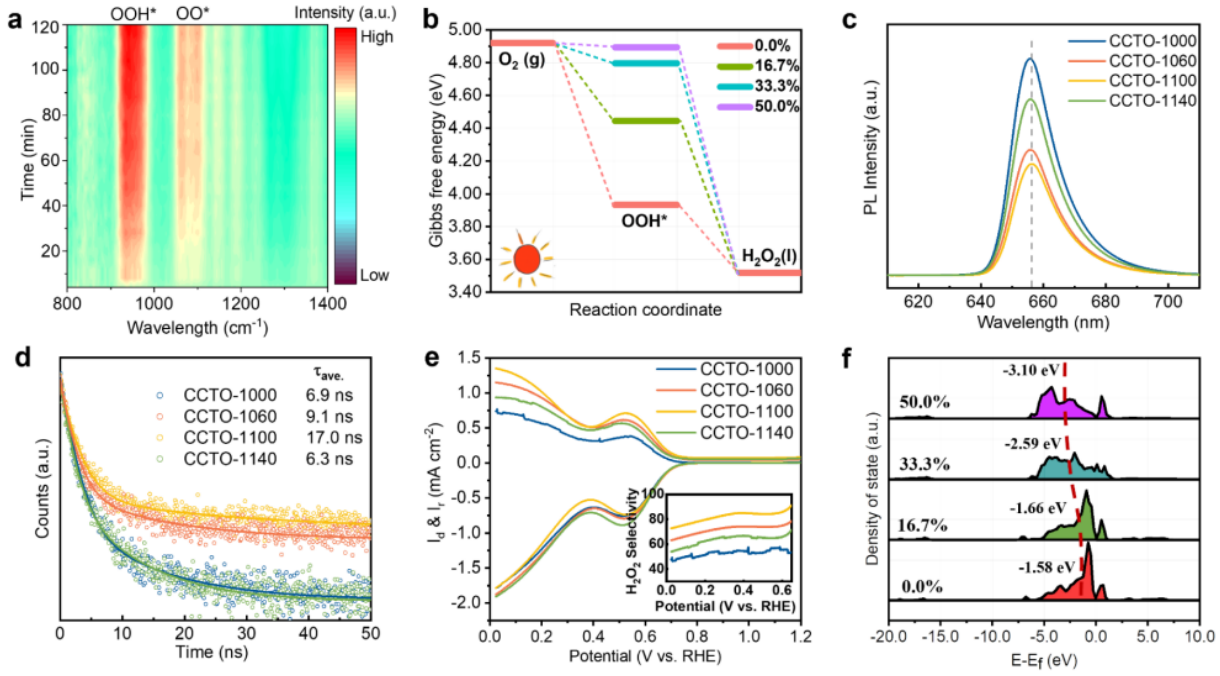


Figure 5. Mechanistic investigation. (a) Synchrotron in situ FT-IR of photocatalytic ORR over CCTO-1100; (b) Gibbs free energy of coordinate with external potential of 0.7 V; (c) PL spectra of CCTO; (d) TR-PL spectra and fittings of CCTO; (e) linear sweep voltammetry curves on RRDE of CCTO, inset is the calculated H2O2 selectivity; (f) calculated density of states of CCTO with varied Cu vacancy content.